Contents

1 Theory **3**
- 1.1 Sesquioxides . . . 3
  - 1.1.1 Chromium Oxide . . . 4
  - 1.1.2 Gallium Oxide . . . 7
- 1.2 X-ray Diffraction Principles . . . 8
  - 1.2.1 Scattering at Lattices . . . 8
  - 1.2.2 X-rays . . . 10
- 1.3 Heteroepitaxy . . . 10
  - 1.3.1 Pseudomorphic Growth . . . 10
  - 1.3.2 Relaxed Growth . . . 12
    - Dislocations . . . 12
    - Slip Systems for Sesquioxide Heterostructures . . . 13

2 Experimental Methods **15**
- 2.1 Pulsed Laser Deposition . . . 15
  - 2.1.1 Setup . . . 16
  - 2.1.2 Plasma Dynamics . . . 16
  - 2.1.3 Segmented Target Approach . . . 18
- 2.2 X-Ray Diffraction Measurement . . . 18
  - 2.2.1 2θ-ω-scans . . . 19
  - 2.2.2 ω-scans . . . 20
  - 2.2.3 ϕ-scans . . . 21
  - 2.2.4 Reciprocal Space Maps . . . 21
  - 2.2.5 Technical Details . . . 23
- 2.3 Further Methods . . . 24
  - 2.3.1 Thermal Evaporation . . . 24
  - 2.3.2 Resistivity Measurement . . . 25
  - 2.3.3 Thickness Determination . . . 26
  - 2.3.4 Spectral Transmission . . . 27

3 Experiment, Results and Discussion **29**
- 3.1 Preliminary Investigations . . . 30
  - 3.1.1 Experiment . . . 30
  - 3.1.2 Results . . . 30
    - Oxygen Partial Pressure Variation on m-plane Sapphire . . . 30
    - Growth Temperature Variation on m-plane Sapphire . . . 33
    - Influence of Growth Rate on Crystal Structure . . . 34

Deposition on *c*-, *r*-, *m*- and *a*-plane Sapphire . . . 37
3.1.3 Conclusion . . . 39
3.2 Doping of Cr_2O_3 Thin Films . . . 41
3.2.1 Experiment . . . 41
3.2.2 Results . . . 42
Laser Position Variation for Different Targets . . . 42
Ohmic Contact Optimization . . . 49
3.2.3 Conclusion . . . 49
3.3 Strain Analysis . . . 51
3.3.1 Experiment . . . 51
Sample Fabrication . . . 51
Measurements . . . 52
3.3.2 Results . . . 54
c-plane: Laser Spot Size Variation . . . 56
c-plane: Pulse Energy Variation . . . 58
r-plane: Laser Spot Size Variation . . . 60
r-plane: Pulse Energy Variation . . . 61
m- and *a*-plane: Laser Spot Size Variation . . . 63
m- and *a*-plane: Pulse Energy Variation . . . 64
3.3.3 Conclusion . . . 67
3.4 Cr_2O_3 Buffer Layers for α-Ga_2O_3 . . . 69
3.4.1 Experiment . . . 69
3.4.2 Results . . . 70
3.4.3 Conclusion . . . 74

Appendices **77**

A Calculations **79**
A.1 *m*-plane lattice constants . . . 79
A.2 *a*-plane lattice constants . . . 80

B Figures **81**

Bibliography **87**

Chapter 3

Experiment, Results and Discussion

Contents

3.1 Preliminary Investigations 30
3.1.1 Experiment 30
3.1.2 Results 30
3.1.3 Conclusion 39
3.2 Doping of Cr_2O_3 Thin Films 41
3.2.1 Experiment 41
3.2.2 Results 42
3.2.3 Conclusion 49
3.3 Strain Analysis 51
3.3.1 Experiment 51
3.3.2 Results 54
3.3.3 Conclusion 67
3.4 Cr_2O_3 Buffer Layers for α-Ga_2O_3 69
3.4.1 Experiment 69
3.4.2 Results 70
3.4.3 Conclusion 74

3.1 Preliminary Investigations

In the following, the feasibility of depositing Cr_2O_3 thin films via Pulsed Laser Deposition (PLD) as well as their resulting physical properties are investigated. Because Cr_2O_3 is the most stable chromium oxide, its formation is expected, but other oxidation states cannot be excluded. E.g., in Fig. 3.14, a silver colored target coating can be observed, presumably corresponding to metallic CrO_2. If Cr_2O_3 is the only oxidation state, then amorphous or rhombohedral films are expected, because no other polymorph of Cr_2O_3 exists. Furthermore, if a crystalline phase is present, the orientation with respect to the sapphire substrates is of interest. Because Al_2O_3 and Cr_2O_3 exhibit the same crystal symmetry, it is expected that the crystal orientation of the film matches the corresponding substrate orientation. Finally, deposition parameters should be optimized to obtain the best crystal quality.

3.1.1 Experiment

Due to the similar crystal structure of Cr_2O_3 and α-Ga_2O_3, the deposition parameters of the latter were chosen as a starting point to deposit chromia thin films on $10 \times 10\,\mathrm{mm}^2$ sapphire substrates with m-plane orientation [**petersen2023**]. Namely, a pulse energy of 650 mJ and a pulse frequency of 20 Hz were applied for a total of 30 000 pulses. To investigate the influence of deposition parameters, three batches were produced:

1. variation of oxygen partial pressure $p(O_2)$ from 8×10^{-5} to 1×10^{-2} mbar with a fixed temperature of 745 °C,

2. variation of growth temperature from 725 to 765 °C with a fixed oxygen partial pressure of 1×10^{-3} mbar, and

3. variation of substrate orientation between c- (00.1), r- (01.2) m- (10.0) and a-plane (11.0) $5 \times 5\,\mathrm{mm}^2$ sapphire substrates[(1)] with a fixed oxygen partial pressure of 1×10^{-3} mbar and a growth temperature of 715 °C.

Structural properties of those thin films were determined by 2θ-ω-scans, ω-scans and ϕ-scans. The thickness was determined via spectroscopic ellipsometry, and transmission spectra were recorded for two samples of the 1st batch to determine the optical band gap. By dividing the thickness by the number of applied pulses, the growth rate g can be calculated as is provided in units of $\mathrm{pm\,pulse}^{-1}$. Temperature dependent resistivity measurements were performed only for the samples of the 3rd batch, because all m-plane oriented samples showed no conductivity at room temperature.

3.1.2 Results

Oxygen Partial Pressure Variation on *m*-plane Sapphire

In the following, the results for the samples produced at four different oxygen partial pressures are analyzed. In Fig. 3.2, the 2θ-ω-patterns are depicted. For each pattern, the two peaks (solid line) at around 68° correspond to the (30.0) reflection of the m-plane oriented sapphire substrate. The splitting occurs due to the similar wavelength of

(1) In the following, the Bravais-Miller-indices will be omitted.

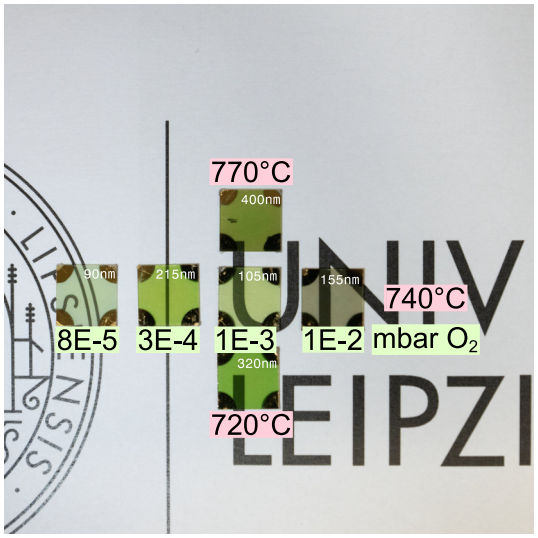

Figure 3.1: Image of the samples produced at different oxygen partial pressures ($T = 740\,^{\circ}\mathrm{C}$) and different growth temperatures ($p(\mathrm{O_2}) = 1 \times 10^{-3}\,\mathrm{mbar}$).

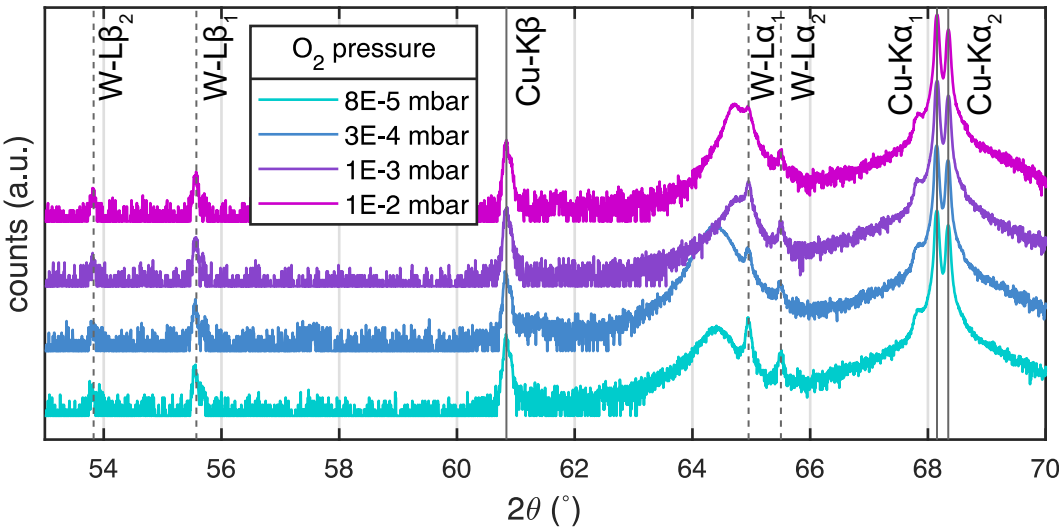

Figure 3.2: 2θ-ω-patterns of Cr_2O_3 thin films deposited on m-plane sapphire for various oxygen partial pressures. The solid lines indicate (30.0) substrate reflections corresponding to copper radiation, whereas the dashed lines indicate (30.0) substrate reflections corresponding to tungsten radiation.

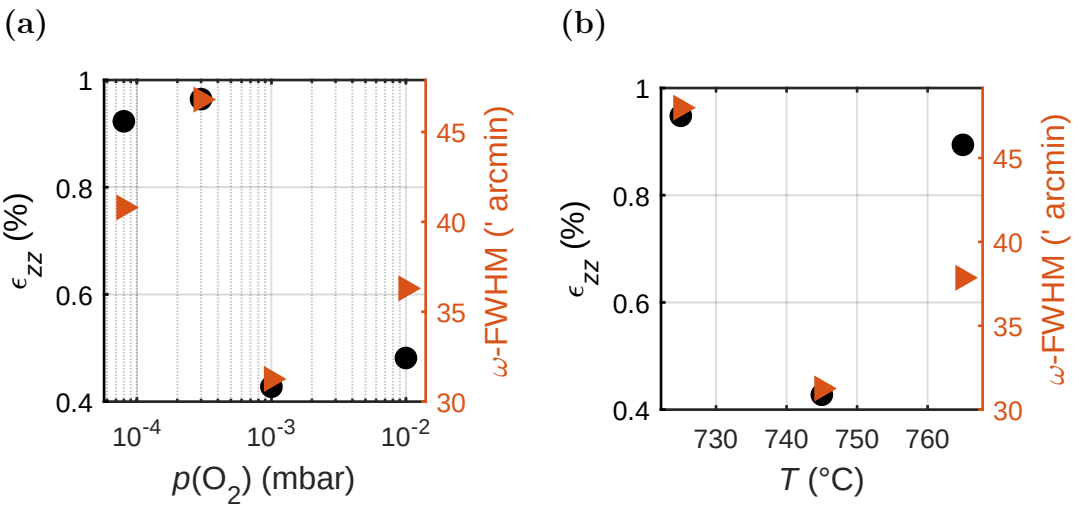

Figure 3.3: **(a)** Out-of-plane Strain and ω-FWHM for the samples fabricated at different oxygen pressures. **(b)** Out-of-plane Strain and ω-FWHM for the samples fabricated at different growth temperatures.

Cu-Kα_1 and Cu-Kα_2 radiation. The additional peaks also stem mainly from the (30.0) reflection of Al_2O_3 and are caused by W-Lβ_2-, W-Lβ_1-, Cu-Kβ-, W-Lα_1- and W-Lα_2-radiation (increasing angles). In the vicinity of the calculated peak position for the (30.0) reflection of Cr_2O_3 (cf. 1.4), there is a peak observed for each sample, indicating that the α-phase of Cr_2O_3 is present. Note that the peak position is varying depending on the chosen oxygen partial pressure. The difference to the expected peak position $2\theta_0$ is expressed as out-of-plane (o.o.p.) strain ϵ_{zz} using the Bragg equation Equ. (1.10) and then

$$\epsilon_{zz} = \frac{d - d_0}{d_0} = \left(\frac{1}{\sin(2\theta/2)} - \frac{1}{\sin(2\theta_0/2)} \right) \cdot \sin(2\theta_0/2)\,. \tag{3.1}$$

In Fig. 3.3a, the calculated strain is shown in dependence of the corresponding oxygen partial pressure (black circles). The strain decreases from approx. 0.95 % to 0.45 % with increasing pressure. This strain reduction may therefore be the result of increased background gas scattering which results in less kinetic energy of the specimen reaching the heated substrate (cf. 2.1.1).

For each sample, the 2θ angle was fixed to the observed (30.0) reflection of Cr_2O_3 and an ω-scan was performed. The Full Width at Half Maximum (FWHM) of the ω-patterns (henceforth *ω-FWHM*) are depicted in Fig. 3.3a (orange triangles). The values vary between approx. 30′ and 50′ and show a dependence on oxygen partial pressure, which is less pronounced compared with o.o.p. strain. Still, since ω-FWHM is connected to the mosaicity of the thin film, higher oxygen partial pressures yield slightly better crystal qualities. Note that due to the fact that an oxygen partial pressure of 1×10^{-3} mbar yielded the best crystal quality, this value is used for future deposition processes.

To probe for rotational domains of the thin films, ϕ-scans were performed by fixing 2θ and ω to the corresponding angles of the (30.6) plane of Cr_2O_3, which has an inclination angle of 32.4° with respect to the (30.0) plane. The diffraction patterns are depicted in Fig. 3.4. The observed peaks of the thin film align with the peaks of the single crystal substrate, indicating that the film has no in-plane rotation with respect to the

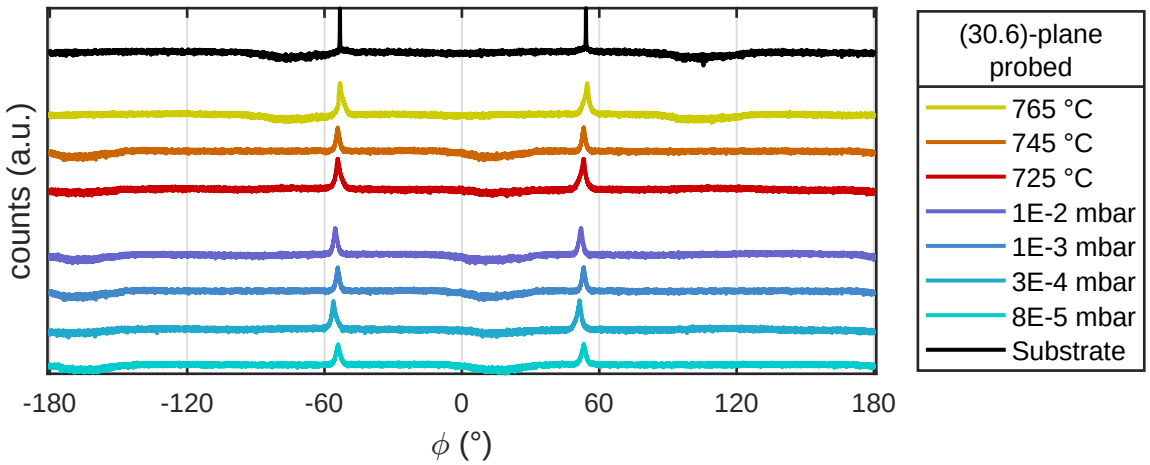

Figure 3.4: Diffraction patterns of ϕ-scans performed on the inclined (30.6) reflection for m-plane oriented Cr_2O_3 samples (color). The corresponding pattern of the Al_2O_3 substrate is also depicted (black). The diffraction patterns cover the samples from variation of oxygen partial pressure (teal to blue colored) and variation of growth temperature (red to yellow colored).

substrate. Furthermore, the absence of additional peaks indicates that there exists only a single domain of the thin film.

The growth rate g varies between 3 pm pulse^{-1} and 7 pm pulse^{-1} and is depicted in Fig. 3.5a. No systematic dependence on the oxygen partial pressure can be observed. This is not expected, because the background pressure is related to scattering of the plasma species, which should alter the kinetic energy and therefore the growth dynamics. This behavior is attributed to reduced laser fluence on the target due to window coating, as it will be explained below.

The transmission spectra of two selected Cr_2O_3 thin films are shown in Fig. 3.6a. The samples are not fully transparent in the visible spectrum (80 % transmission at 400 nm) and they exhibit a green tint, as can also be seen in Fig. 3.1. To determine the onset of absorption E_{opt}, an α^2 vs. E plot (Fig. 3.6b) is utilized (cf. 2.3.4). Although the publications used for reference in this work support the direct transition nature of Cr_2O_3 [**mi2018**, 17], it has to be noted that there exist studies determining the optical band gap of Cr_2O_3 by assuming an indirect transition nature [14, 15]. However, all of them utilize a Tauc plot $(\alpha E)^\eta$ vs. E, which is an unappropriate method for crystalline solids as discussed in 2.3.4. Therefore, the method based on the assumption of parabolic shape of bands as well as direct transitions (cf. 2.3.4) is used. Fitting the linear regime between 3.75 eV and 4.3 eV results in $E_{opt} \approx 3.6$ eV for both samples, which differ in strain and ω-FWHM by a factor of approx. 2 and 0.3, respectively. A second absorption edge can be identified between 5.3 eV and 5.5 eV and yields an optical gap of $E_{opt} \approx 5.1$ eV for both samples.

Growth Temperature Variation on m-plane Sapphire

In the following, the results for the three samples produced at different growth temperatures are presented. Similar to the previous results, the (30.0) reflection of the α-phase of Cr_2O_3 can be observed (Fig. 3.7). The calculated o.o.p. strain is shown in

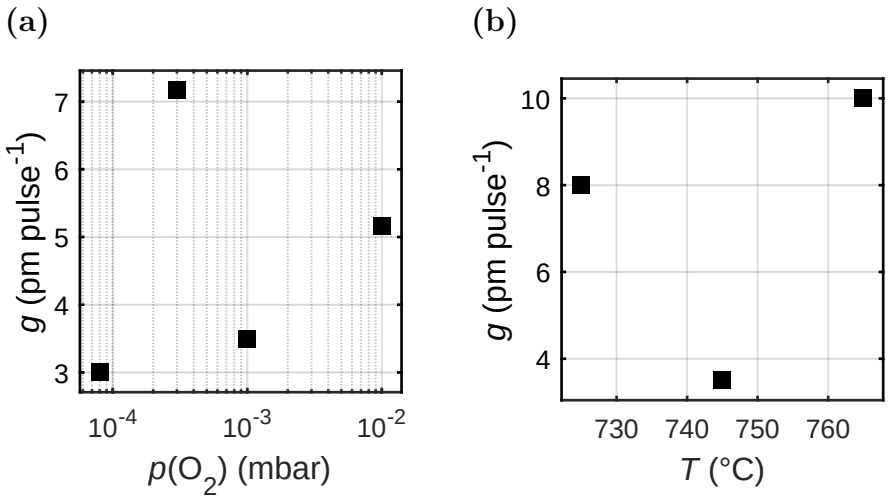

Figure 3.5: Growth rates g for the samples fabricated with **(a)** varying oxygen pressure and **(b)** varying growth temperature.

Fig. 3.3b and a large spread of strain can be observed, varying between 0.4 % and 1 %. Note that there is no systematic dependence on growth temperature. The ω-FWHMs of the Cr_2O_3 (30.0) reflection are shown in Fig. 3.3b and exhibit a similar spread as the samples with varying oxygen partial pressure, but similar to the o.o.p. strain, no dependence on growth temperature is observed. The ϕ-scans (Fig. 3.4) show that the thin films are in-plane aligned with the respective substrate and that no rotational domains are present. Finally, the growth rate varies between 3.5 pm pulse^{-1} and 10 pm pulse^{-1} with no observable dependence on growth temperature.

Influence of Growth Rate on Crystal Structure

It has to be noted that there is a large spread in strain and ω-FWHM for the samples that were deposited at different growth temperatures. The range of temperature variation was only 40 °C and has no significant influence on the distribution of strain and ω-FWHM (Fig. 3.3b). Because all the other process parameters were kept the same[(2)], this indicates that another parameter influences the crystal quality. This is supported by the fact that the growth rate correlates with the magnitude of strain and ω-FWHM, as can be seen in Fig. 3.8a (the outlier with low growth rate but high strain will be explained below). Note that at this point, the growth rate cannot be deconvoluted from the thin film thickness. Therefore, it is not clear whether the thickness influences the crystal quality or the reduced growth rate due to the reasons explained below.

The origin of the varying growth rate – and therefore varying crystal quality – can be found when taking the number of processes into account that were performed before. In Fig. 3.8b, the growth rate is visualized depending on the order of sample fabrication. It is also indicated when the laser entrance window has been cleaned. It is common practice to clean the latter every couple of processes due to coating with target material which absorbs laser energy. E.g., in the case of ZnO, even after 100 000 pulses, no significant influence can be observed on the transmission of laser energy. But from

(2) In fact, for the last two samples produced (T = 725 °C and T = 765 °C), the pulse number was increased to 40 000 pulses. This was due to the fact that the growthrate decreased.

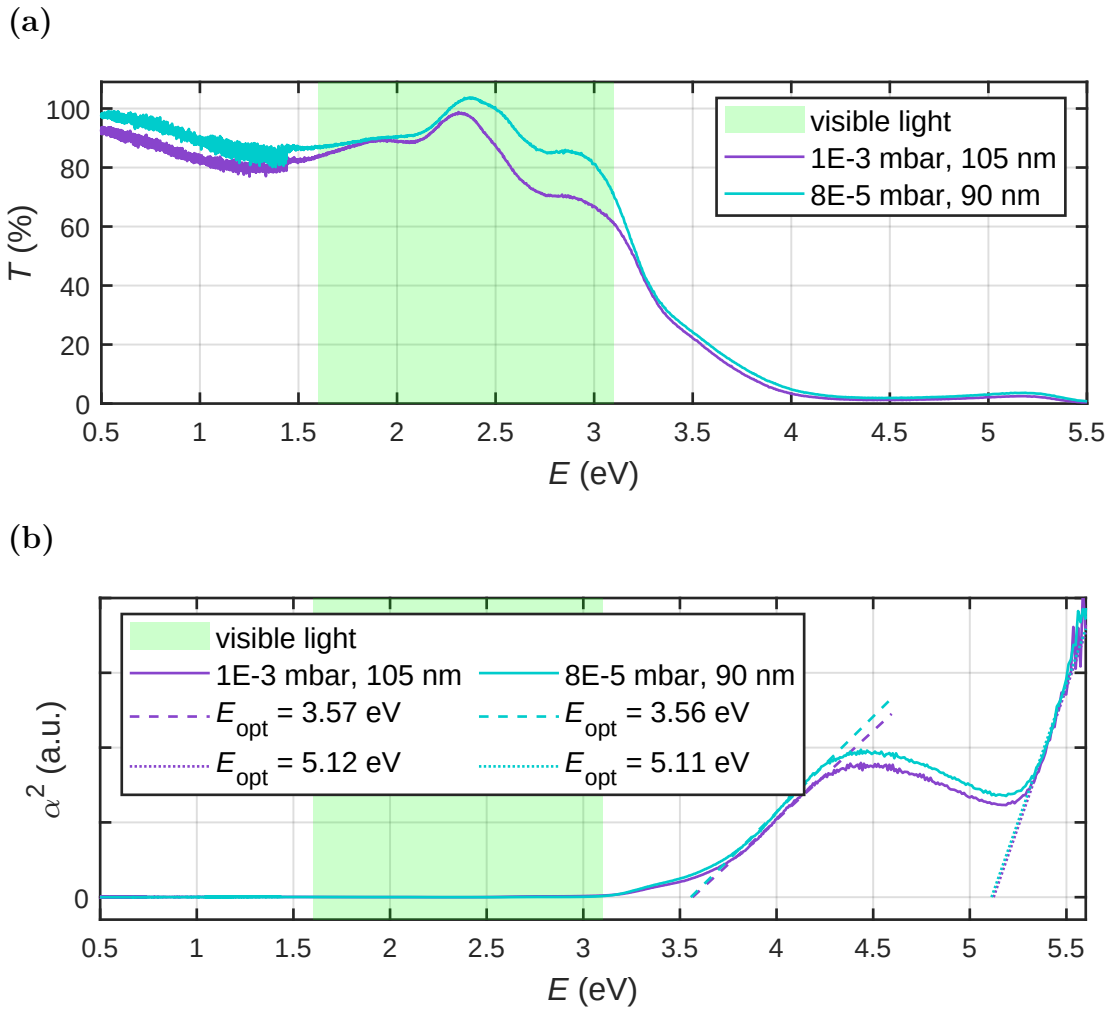

Figure 3.6: **(a)** Transmission spectra of two selected Cr_2O_3 thin films, deposited with different oxygen partial pressures of 1×10^{-3} mbar and 8×10^{-5} mbar. The spectra are normalized to a corresponding uncoated m-plane sapphire substrate. No correction to film thickness was done, which results in a lower transmittance of the thicker sample (purple). **(b)** α^2 vs. E plot of the above-mentioned samples. It is assumed that Cr_2O_3 has a direct bandgap [**mi2018**, 17]. The fitting regime for determining the optical gap is chosen to be between 3.75 eV and 4.3 eV, as well as between 5.3 eV and 5.5 eV.

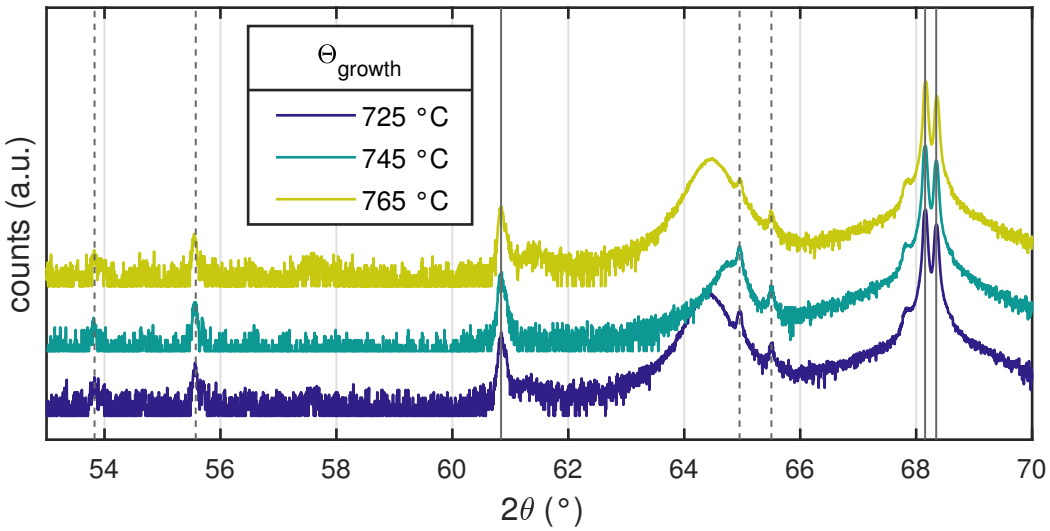

Figure 3.7: 2θ-ω-pattern of Cr_2O_3 thin films deposited on m-plane sapphire for three different growth temperatures. The lines indicate substrate reflections that stem from copper and tungsten radiation (cf. 3.2)

Fig. 3.8b it becomes clear that this should be done much more frequently when working with Cr_2O_3. Note that the laser has a wavelength of 248 nm, corresponding to 5.0 eV, which is not transmitted by Cr_2O_3 thin films[(3)], as can be seen in Fig. 3.6a. Therefore, the increasing coating of the laser entrance window with each new process absorbs a large amount of laser pulse energy, resulting in less fluence on the PLD target. This results in less ablated target material and less kinetic energy of the ablated species, which leads to a reduced growth rate and different crystal growth conditions that have higher strain and ω-FWHM as a result.

This explanation is supported by the dependence of crystal quality on oxygen partial pressure (cf. Fig. 3.3a). There, the increment of crystal quality with higher oxygen pressures is attributed to the increased background gas scattering resulting in less kinetic energy of the plasma material. This also explains the outlier in Fig. 3.8a, where one sample corresponds to a higher strain and ω-FWHM of approx. 0.9 % and 41′, respectively (black square). This is not expected when considering the rather small growth rate of 3 pm pulse^{-1} (`W6724` in Fig. 3.8b). But when taking account for the fact that this sample is fabricated at a very low oxygen partial pressure of 8×10^{-5} mbar, it becomes clear that although the reduced fluence on the target would generally lower the kinetic energy of the plasma material, the limited scattering with the background gas counteracts this effect, resulting in the observed crystal quality.

It is noteworthy that the observed strain (cf. Fig. 3.3a,b) is distributed around two distinct values of approx. 0.4 % and 0.9 %. A prior reported thin film tilt for m-plane oriented rhombohedral heterostructures [7] may be the reason for this observation: the samples are installed in the XRD device in such a way that the c-axis is either parallel or orthogonal to the scattering plane. This orientation is arbitrary, and thus the (expected) thin film tilt is either along the X-ray beam or perpendicular to it, which could result in

(3) To be precise, the transmission spectrum in Fig. 3.6a is recorded for m-plane oriented *crystalline* Cr_2O_3 thin films. This may not be the present phase when Cr_2O_3 deposits on the (colder) window made out of glass, where it may form an amorphous phase.

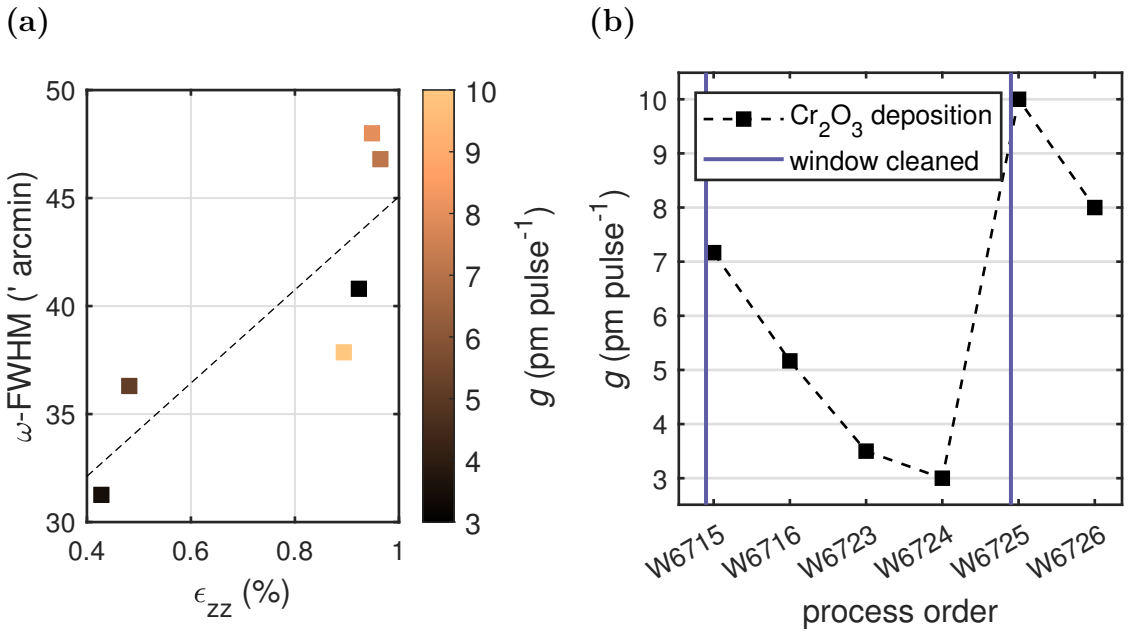

Figure 3.8: **(a)** Correlation of ω-FWHM with o.o.p. strain, as well as correlation of both with growth rate g (false color). The dashed line is a linear fit serving as guide to the eye. The outlier with low growth rate but large strain can be explained by accounting for the low oxygen partial pressure of 8×10^{-5} mbar for this sample. This results in larger kinetic energy of the plasma species. **(b)** Growth rate depending on order of sample fabrication.

unexpected results when calculating the o.o.p. lattice plane distance from the observed peak position. To check if this is the origin of the observed strain, for two samples of different strain according to Fig. 3.3, four 2θ-ω-scans were performed with incrementing the azimuth by 90° after each measurement. The resulting diffraction patterns are depicited in Fig. 3.9. The strain is independent of azimuth, only the peak intensity is altered by the in-plane rotation of the sample as expected. For both samples, an azimuth of 0° and 180° results in a lower intensity, supporting the hypothesis that the (expected) thin film tilt is perpendicular to scattering plane which results in a deviation from the Bragg condition. Therefore, the distribution of observed strain is not a measurement artifact.

Deposition on *c*-, *r*-, *m*- and *a*-plane Sapphire

For the samples deposited on substrates with different orientation, 2θ-ω-patterns were recorded (Fig. 3.10). For each sample, the expected substrate peaks are observed: (00.6) and (00.12) for *c*-plane; (01.2), (02.4), (03.6) and (04.8) for *r*-plane; (30.0) for *m*-plane; (11.0) and (22.0) for *a*-plane. Several smaller peaks also correspond to those reflections but stem from other X-rays than Cu-Kα (cf. Fig. 3.2). The mentioned reflections are also observed for the Cr_2O_3 thin film, but with a shift in 2θ position similar to the previously investigated *m*-plane samples (Tab. 3.1). Note that for *r*-plane, the higher order reflections of Cr_2O_3 cannot be observed. It can be concluded that Cr_2O_3 grows in the α-phase on sapphire substrates of different orientation, where the thin film orientation matches the corresponding substrate. Henceforth, "*c*-plane Cr_2O_3" will refer to a Cr_2O_3 thin film deposited on *c*-plane oriented $5 \times 5\,\mathrm{mm}^2$ sapphire substrates, and so

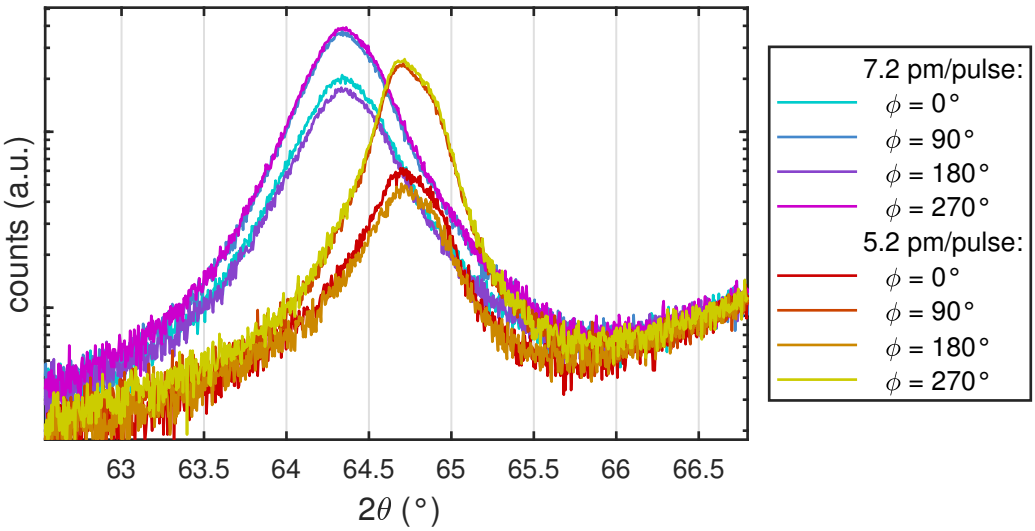

Figure 3.9: 2θ-ω-patterns for two samples in four different azimuths each.

Table 3.1: Structural parameters, approximate resistivity at room temperature and activation energy for Cr_2O_3 thin films of different orientation.

Plane	ϵ_{zz} (%)	ω-FWHM ($'$)	ρ (Ω cm)	E_A (meV)
c	1.71	42.6	3	57, 34
r	0.72	38.4	120	117
m	0.55	42.6	3600	240
a	1.41	32.4	4900	259

on. For each sample, ω-scans were performed on the (00.6), (02.4), (30.0) and (11.0) reflections for c-, r-, m- and a-plane, respectively. The resulting ω-FWHMs are in the range of approx. $30'$ to $40'$ (Tab. 3.1).

Because the resistivity of all samples was too high to measure Hall effect, only resistivity measurements (cf. 2.3.2) were performed for several temperatures (Fig. 3.11). The samples were contacted on four corners with Ti-Al-Au via thermal evaporation. The resistivity depends strongly on the orientation of the thin film, the resistivities at room temperature are listed in Tab. 3.1. A difference of more than three orders of magnitude between c-plane and a-plane samples is observed. The linear behavior of the ARRHENIUS-plot[4] indicates a thermally activated mechanism for conductivity, and thus semiconductive behavior. Note that no further conclusions can be drawn on the conduction mechanisms due to the missing carrier concentration and mobility data. By assuming a behavior of the form

$$\rho \propto \exp\left(\frac{E_A}{k_B T}\right) , \tag{3.2}$$

with BOLTZMANN constant k_B, an activation energy E_A can be estimated. Those energies are also listed in Tab. 3.1. For c-plane Cr_2O_3, two linear regimes can be dis-

[4] Visualization of $f(T)$ as $f'(\tau)$ with $f' = \log f$ and $\tau = 1/T$.

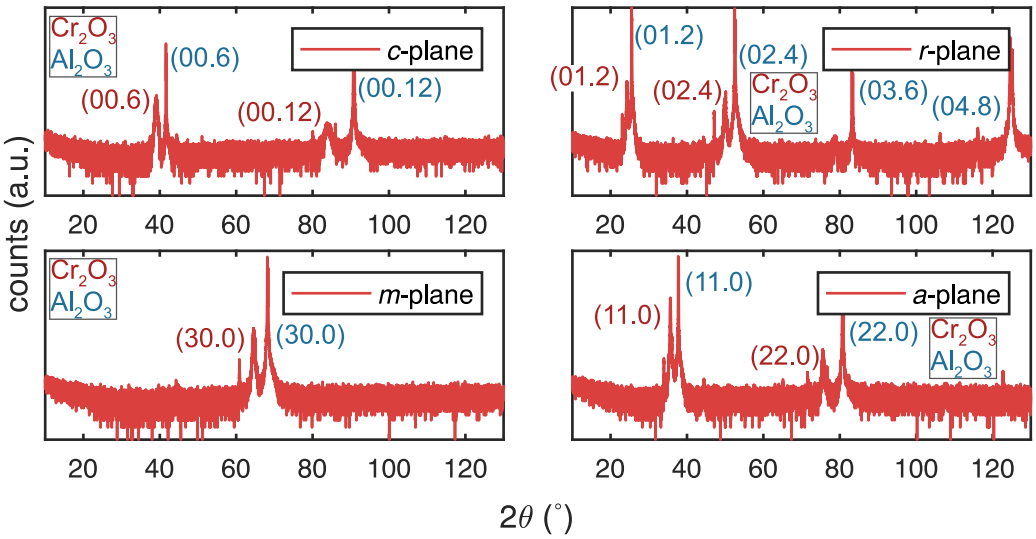

Figure 3.10: 2θ-ω-patterns of Cr_2O_3 thin films deposited on *c*-, *r*-, *m*- and *a*-plane sapphire.

tinguished, favoring a dependence of the form

$$\rho \propto a \exp\left(\frac{E_{A,1}}{k_B T}\right) + b \exp\left(\frac{E_{A,2}}{k_B T}\right) , \tag{3.3}$$

thus two activation energies are determined. In previous studies, activation energies of 400 to 500 meV for polycrystalline Cr_2O_3 thin films prepared by Chemical Vapor Deposition (CVD) [14] and 200 meV for Mg-doped *c*-plane thin films prepared by electron beam Physical Vapor Deposition (PVD) evaporation [17] were reported. The values were also determined by simply fitting the linear regime in an ARRHENIUS plot of the conductivity.

3.1.3 Conclusion

m-plane Cr_2O_3 thin films can be deposited over a wide range of oxygen partial pressure of more than 2 orders of magnitude. It turned out that the crystal quality correlates mainly with the growth rate which is presumably subject to a variation of the laser pulse fluence on the target. Therefore, lower kinetic energy of the plasma species is probably the reason for improved crystallinity and less strain. Even though the influence of those parameters was less dominant, an oxygen partial pressure of 1×10^{-3} mbar and a growth temperature of 750 °C are identified as best growth conditions. Note that those values overlap with the conditions for deposition α-Ga_2O_3, which makes ternary solid solutions of chromia with rhombohedral Ga_2O_3 feasible.

α-Cr_2O_3 could also deposited on *c*-, *r*- and *a*-plane sapphire, with the thin films crystallizing in the respective orientation. This is important for heterostructures with α-$Ga_2O_3$and could enable growth of rhombohedral Ga_2O_3 on all common sapphire cuts via Cr_2O_3 buffer layers. Note that all deposited thin films showed a discrepancy between observed o.o.p. lattice constants and bulk Cr_2O_3 literature values (Tab. 1.1). The conductivity is strongly dependent on the crystal orientation and was very low for the prismatic orientations, but with 0.3 S cm^{-1} three orders of magnitude higher for the basal orientation.

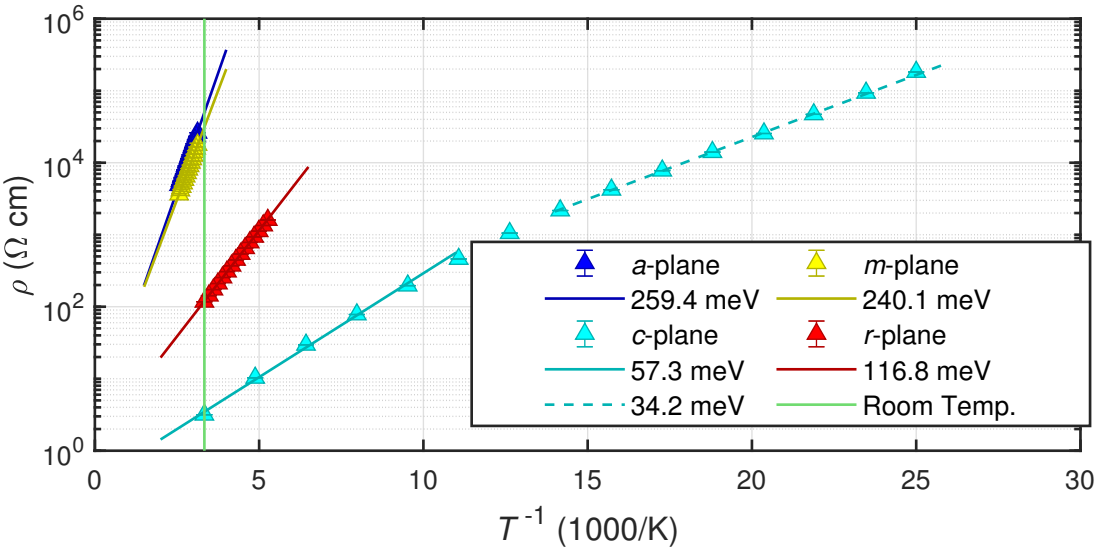

Figure 3.11: Temperature dependent resistivity measurements for samples with different orientations.

Bibliography

[1] Michael Lorenz. "Pulsed laser deposition". In: *Encyclopedia of Applied Physics*. Wiley, 2019. URL: http://dx.doi.org/10.1002/3527600434.eap810.

[2] Holger von Wenckstern *et al.* "A review of the segmented-target approach to combinatorial material synthesis by pulsed-laser deposition". In: *Phy. Status Solidi B* 257.7 (2020), p. 1900626. ISSN: 0370-1972, 1521-3951. DOI: 10.1002/pssb.201900626.

[3] George F. Harrington and José Santiso. "Back-to-Basics tutorial: X-ray diffraction of thin films". In: *Journal of Electroceramics* 47.4 (2021), pp. 141–163. ISSN: 1385-3449, 1573-8663. DOI: 10.1007/s10832-021-00263-6.

[4] V. Srikant, J. S. Speck, and D. R. Clarke. "Mosaic structure in epitaxial thin films having large lattice mismatch". In: *Journal of Applied Physics* 82.9 (1997), pp. 4286–4295. ISSN: 0021-8979, 1089-7550. DOI: 10.1063/1.366235.

[5] Marius Grundmann. "Elastic theory of pseudomorphic monoclinic and rhombohedral heterostructures". In: *Journal of Applied Physics* 124.18 (2018), p. 185302. ISSN: 0021-8979, 1089-7550. DOI: 10.1063/1.5045845.

[6] M. Grundmann and M. Lorenz. "Anisotropic strain relaxation through prismatic and basal slip in α-(Al, Ga)$_2$O$_3$ on R-plane Al$_2$O$_3$". In: *APL Materials* 8.2 (2020), p. 021108. ISSN: 2166-532X. DOI: 10.1063/1.5144744.

[7] Max Kneiß *et al.* "Strain states and relaxation for α-(Al$_x$Ga$_{1-x}$)$_2$O$_3$ thin films on prismatic planes of α-Al$_2$O$_3$ in the full composition range: Fundamental difference of a- and m-epitaxial planes in the manifestation of shear strain and lattice tilt". In: *Journal of Materials Research* 36.23 (2021), pp. 4816–4831. ISSN: 0884-2914, 2044-5326. DOI: 10.1557/s43578-021-00375-3.

[8] Sofie Vogt *et al.* "Realization of Conductive n-Type Doped α-Ga$_2$O$_3$ on *m*-Plane Sapphire Grown by a Two-Step Pulsed Laser Deposition Process". In: *physica status solidi (a)* 220.3 (2023), p. 2200721. ISSN: 1862-6300, 1862-6319. DOI: 10.1002/pssa.202200721.

[9] L. J. van der Pauw. "A method of measuring specific resistivity and Hall effect of discs of arbitrary shape". In: *Philips Research Reports* 13.1 (1958), pp. 1–9.

[10] Hiroyuki Fujiwara. *Spectroscopic Ellipsometry. Principles and Applications*. Tōkyō: John Wiley & Sons, Ltd, 2007. ISBN: 978-4-621-07253-0.

[11] J.C. Manifacier *et al.* "Optical and electrical properties of SnO2 thin films in relation to their stoichiometric deviation and their crystalline structure". In: *Thin Solid Films* 41.2 (1977), pp. 127–135. ISSN: 00406090. DOI: 10.1016/0040-6090(77)90395-9.

[12] A. R. Zanatta. "Revisiting the optical bandgap of semiconductors and the proposal of a unified methodology to its determination". In: *Scientific Reports* 9.1 (2019), p. 11225. ISSN: 2045-2322. DOI: 10.1038/s41598-019-47670-y.

[13] Jan Tauc. "Optical properties of amorphous semiconductors and solar cells". In: *Fundamentals of Semiconductors*. 3rd ed. Berlin, Heidelberg: Springer, 2005. ISBN: 3-540-41323-5.

[14] Chun-Shen Cheng, H. Gomi, and H. Sakata. "Electrical and Optical Properties of Cr_2O_3 Films Prepared by Chemical Vapour Deposition". In: *Physica Status Solidi (a)* 155.2 (1996), pp. 417–425. ISSN: 00318965, 1521396X. DOI: 10.1002/pssa.2211550215.

[15] M.F. Al-Kuhaili and S.M.A. Durrani. "Optical properties of chromium oxide thin films deposited by electron-beam evaporation". In: *Optical Materials* 29.6 (2007), pp. 709–713. ISSN: 09253467. DOI: 10.1016/j.optmat.2005.11.020.

[16] Jarnail Singh *et al.* "Structural, optical and electrical characterization of epitaxial Cr_2O_3 thin film deposited by PLD". In: *Materials Research Express* 6.10 (2019), p. 106406. ISSN: 2053-1591. DOI: 10.1088/2053-1591/ab3543.

[17] L. Farrell *et al.* "Conducting mechanism in the epitaxial *p*-type transparent conducting oxide Cr_2O_3:Mg". In: *Physical Review B* 91.12 (2015), p. 125202. ISSN: 1098-0121, 1550-235X. DOI: 10.1103/PhysRevB.91.125202.

[18] Alex Dolgonos, Thomas O. Mason, and Kenneth R. Poeppelmeier. "Direct optical band gap measurement in polycrystalline semiconductors: A critical look at the Tauc method". In: *Journal of Solid State Chemistry* 240 (2016), pp. 43–48. ISSN: 00224596. DOI: 10.1016/j.jssc.2016.05.010.